JOURNAL OF PROPULSION AND POWER
Vol. 24, No. 4, July–August 2008

Wear Mechanisms in Electron Sources for Ion Propulsion, 1: Neutralizer Hollow Cathode

Ioannis G. Mikellides* and Ira Katz†
Jet Propulsion Laboratory, California Institute of Technology, Pasadena, California 91109

DOI: 10.2514/1.33461

Upon the completion of two long-duration life tests of a 30-cm ion engine, the orifice channel of the neutralizer hollow cathode was eroded away to as much as twice its original diameter. Whereas the neutralizer cathode orifice opened significantly, no noticeable erosion of the discharge cathode orifice was observed. No quantitative explanation of these erosion trends has been established since the completion of the two life tests. A two-dimensional model of the partially ionized gas inside these devices has been developed and applied to the neutralizer hollow cathode. The numerical simulations show that the main mechanism responsible for the channel erosion is sputtering by Xe^+. These ions are accelerated by the sheath along the channel and bombard the surface with kinetic energy/charge of about 17 V at the beginning of cathode life. The density of the ions inside the neutralizer orifice is computed to be as high as 2.1×10^{22} m^{-3}. Because of the 3.5-times larger diameter of the discharge cathode orifice, the ion density inside the orifice is more than 40 times lower and the sheath drop 7 V lower compared with the values in the neutralizer. At these conditions, Xe^+ can cause no significant sputtering of the surface.

Nomenclature

AW	=	atomic weight
$c_{1,2,3,4}$	=	emitter temperature coefficients
$\mathbf{E}$	=	electric field, V/m
e	=	electron charge, C
$\mathbf{j}$	=	current density, A/m^2
$j_{e,\mathrm{th}}$	=	electron thermal current density, A/m^2
k_B	=	Boltzmann's constant, J/K
L_{ins}	=	length of the emitter insert, m
M	=	mass of xenon ion or atom, kg
m_e	=	mass of electron, kg
N_{AV}	=	Avogadro's number, mol^{-1}
n	=	particle density, particles/m^3
$\hat{\mathbf{n}}$	=	normal unit vector
$\dot{n}$	=	ionization rate, particles/m^3/s
p	=	pressure, Pa
Q^R	=	frictional heating, W/m^3
Q^T	=	thermal heating, W/m^3
r	=	radial coordinate, m
r_o	=	cathode orifice radius, m
T	=	temperature of ionized gas species, K
T_w	=	emitter temperature, K
$T_{w,\max}$	=	peak emitter temperature, K
t	=	time, s
$\mathbf{u}$	=	velocity of ionized gas species, m/s
V_C	=	cathode voltage, V
Y	=	sputtering yield, atoms/ion
z	=	axial coordinate, m
Δh	=	erosion depth or height, m
Δt	=	time increment, h
ε	=	species energy, J
$\varepsilon_{\mathrm{ip}}$	=	ionization potential, V
η	=	electrical resistivity, Ω-m
κ	=	thermal conductivity, W/m/K
λ	=	collision mean free path, m
ν	=	collision frequency, s^{-1}
ρ	=	material mass density, kg/m^3
σ	=	collision cross section, m^2
ϕ	=	plasma potential, V

Subscripts

e	=	electron
e,z	=	electron in z direction
h	=	heavy species (ion or neutral)
i	=	ion
i,z	=	ion in z direction
$i,\perp$	=	ion in direction perpendicular to surface
n	=	neutral
n,z	=	neutral in z direction
p	=	scalar quantity in grid cell center adjacent to boundary

I. Introduction

CATHODE erosion is a major failure mode that is not yet well understood in conventional ring-cusp ion engines. Two long-duration life tests of a 30-cm ion engine were performed by NASA between 1997 and 2004, in part to characterize known failure modes and in part to identify new failure modes. The Life Demonstration Test (LDT) of an engineering model thruster was terminated after 8192 h of operation [1]. During the test, the thruster was operated at the maximum-power (2.3 kW) throttle level, which will be called TH15 in this paper. The Extended-Life Test (ELT) of the Deep Space 1 flight spare ion thruster was conducted from 1998 to 2004 and accumulated 30,352 h [2]. During this test, the engine operated at five different throttle levels that included TH15.

Ring-cusp ion engines such as the 30-cm ion thruster mentioned previously usually operate with two thermionic orificed hollow cathodes: a discharge hollow cathode (DHC) that provides electrons for ionization of the propellant (usually Xe), and a neutralizer hollow cathode (NHC) that provides electrons for the neutralization of the ion beam. The cathode assembly consists mainly of the insert (emitter), cathode tube and orifice plate, heater and radiation shield, keeper tube and plate, cathode insulator, low-voltage propellant

Presented as Paper 5168 at the 43rd AIAA/ASME/SAE/ASEE Joint Propulsion Conference, Cincinnati Duke Energy Convention Center, Cincinnati, OH, 8–11 July 2007; received 15 July 2007; accepted for publication 14 February 2008.

*Member Technical Staff, Electric Propulsion Group, 4800 Oak Grove Drive, Mail Stop 125-109. Senior Member AIAA.

†Group Supervisor, Electric Propulsion Group, 4800 Oak Grove Drive, Mail Stop 125-109. Senior Member AIAA.

isolator, propellant-line screen, and associated wiring and stainless-steel propellant line. A critical function of the keeper is to protect the cathode from degradation by ion bombardment. In the 30-cm ion engine tested during the LDT and ELT, there are two major distinctions between the DHC and NHC (that will be quantified later in the paper): 1) the discharge current is at least a few times higher in the DHC, and 2) the diameter of the orifice channel is approximately 3.5 times larger in the DHC. Each type of cathode used during the LDT was identical to that used in the ELT.

Upon the conclusion of the two life tests, the following observations were made regarding cathode degradation. First, the LDT DHC keeper exhibited a curved erosion pattern along the keeper surface facing the discharge that dipped to a maximum depth of about 500 μm from the location of the original surface. By the end of the ELT, the DHC keeper plate was completely eroded. Second, in both tests, noticeable erosion of the DHC orifice channel walls was absent, but the NHC orifice was eroded to almost twice its original diameter at the exit of the channel. The erosion pattern resembled the divergent section of a de Laval nozzle. Moreover, the erosion patterns in the LDT NHC and the ELT NHC were almost identical by the end of the two tests, suggesting that the erosion of the channel ceased sometime before the termination of the 8200-h test. The mechanisms that led to this erosion and the time by which the erosion ceased have been unknown. This paper presents results from two-dimensional numerical simulations of the NHC that address both questions. In a companion paper, we present computational results related to the erosion of the DHC keeper electrode [3].

The erosion of the NHC orifice channel is a critical life issue for ion propulsion because the sputtered products can lead to channel clogging and/or keeper-to-neutralizer-common shorting. The opening of the channel can also lead to changes in the performance of the cathode, such as loss of flow rate margin, that can in turn lead to "plume mode" operation. Characterized by large oscillations and high coupling voltage, plume mode during flight can lead to the failure of the NHC. Because of the small size of the orifice ($r_o = 140$ μm), access to conventional plasma diagnostics such as probes is extremely difficult. For the NHC in question, no measurements of the plasma inside the orifice region exist. Thus, much of our understanding inside this region must rely on theoretical analyses and numerical simulation.

The partially ionized gas inside these devices is complex and inherently two-dimensional, yet only phenomenological and/or simplified numerical models have been developed. The first attempt to explain the erosion inside the NHC orifice by analytical means was reported by Katz et al. [4], and was an extension of previous idealized work that modeled the plasma inside this region [5]. Katz recognized the significance of the large cross section associated with resonant charge-exchange collisions between low-energy ions and neutrals and developed a one-dimensional diffusion-limited fluid model of the plasma. The orifice model assumed that the ion flow is purely radial, and the axial density gradient terms for ions and neutrals were neglected. An average velocity of neutrals in the channel was determined assuming Poiseuille flow, whereas boundary conditions at the orifice inlet were assumed based on operating conditions. Although no quantitative prediction of the orifice erosion rates was possible, the work suggested that significant erosion can occur when the orifice diameter is as small as in the NHC, largely due to the high degree of ionization that occurs in this region. The importance of the plasma potential on ion acceleration and in turn on the erosion was recognized but its effect was not quantified. Foster et al. [6] proposed a phenomenological model for the production of high-energy ions inside the orifice channel of a DHC that was based upon multiple collisions of ions with the surface. The authors recognized that the dependence of the proposed mechanism on characteristic collision sizes associated with the partially ionized gas warranted numerical simulation. Predictions of observed erosion in support of the proposed mechanism were not performed.

In this paper, we perform fully two-dimensional numerical simulations of the partially ionized gas inside the NHC consisting of electrons, singly charged ions, and neutrals. The computational region spans the emitter, orifice channel and conical regions, and the keeper orifice. The system of conservation laws includes all terms that are believed to drive the evolution of the gas inside these devices, and so no ideal assumptions are made about the ion flow direction, the temperature of the heavy species, or the compressibility of the neutral gas. All dominant collisions between particles (elastic and inelastic) are included. The plasma potential is solved for directly by combining Ohm's law with current conservation, which allows direct predictions of the sheath drop and, in turn, the energy of ions bombarding the cathode surfaces. The plasma solution is used to predict and explain the erosion patterns observed in the two life tests.

II. Neutralizer Hollow Cathode: General Description of the Device and Related Data

The main components of the hollow cathode used in the ion engine life tests are illustrated in Fig. 1. A detailed description of the life test run conditions is provided in [1,2]. Here we provide only the conditions and specifications that are relevant to this study. Both the DHC and NHC contain an impregnated, porous tungsten (W) insert. The insert is housed inside a cathode tube with a W orifice plate welded to the downstream end. A heater coil wrapped around the cathode tube as illustrated in Fig. 1 is used to heat the impregnate and enable ignition by thermionic emission. Table 1 provides a comparison of the DHC and NHC in the 30-cm ion thruster.

The photographs of the neutralizer cathodes after the completion of the two tests (Fig. 2) show that the orifice channel erosion pattern is almost identical in the two NHCs even though the ELT cathode was operated at different throttle levels and for almost four times as long. The patterns in Fig. 2 show little to no erosion at the orifice entrance. The erosion then increases gradually from the orifice entrance to a subtle maximum at about three-fourths of the orifice cylindrical region. Downstream of this point, the erosion appears to exhibit a subtle decrease.

In an environment rich of high-energy ions, erosion may occur as a result of surface sputtering by ion bombardment. The sputtering yield Y for tungsten as a function of xenon ion energy has been measured by Doerner [7] for values as low as 30 V, and is fitted with the function

$$Y(\bar{\varepsilon}_i) = \exp\{-38.744[4.3429\,\ell_n(\bar{\varepsilon}_i) - 9]^{-0.5} + 8.101\} \qquad \bar{\varepsilon}_i = \varepsilon_i/e \tag{1}$$

as shown in Fig. 3 for use in the ensuing erosion calculations. The sputtering yield measurements were obtained by immersing samples in xenon plasma and then biasing the samples relative to the plasma to generate the ion energies of interest. The geometry of the experiment was such that the ions impinged normal to the sample surface. For erosion estimates below 30 V, an extrapolation fit to the

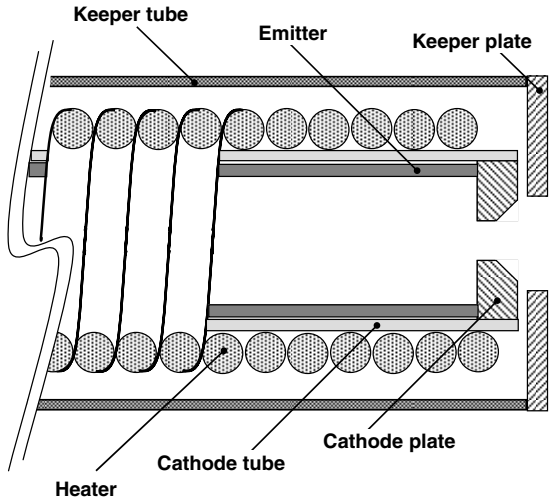

Fig. 1 Schematic of a typical thermionic cathode used in ion propulsion (not to scale).

Table 1 Typical geometrical and operational characteristic ratios of the NHC over the DHC used in the 30-cm ion engine life tests

	Ratio, NHC/DHC
Discharge current [a]	0.245
Mass flow rate [a]	0.973
Cathode tube diameter	1.000
Cathode orifice radius	0.275
Keeper orifice radius	1.000
Orifice (cyl) channel length	1.000
Emitter insert length	1.000

[a]Condition is at the full-power throttle level (TH15).

measurements is used as shown by the dashed line in Fig. 3. The uncertainty in the data for the low-energy values is about ±40% and is illustrated by the error bars in Fig. 3.

III. Theoretical Model

The two-dimensional numerical model solves the fluid conservation laws for three species present in the partially ionized gas: electrons, xenon ions, and xenon neutrals. It is assumed that only singly charged ions are present and that the ionized species satisfy quasi neutrality $n \equiv n_e = n_i$. The computational region employed for the NHC simulations is illustrated in Fig. 4. It is noted that the downstream boundary is the keeper orifice exit. Several preliminary

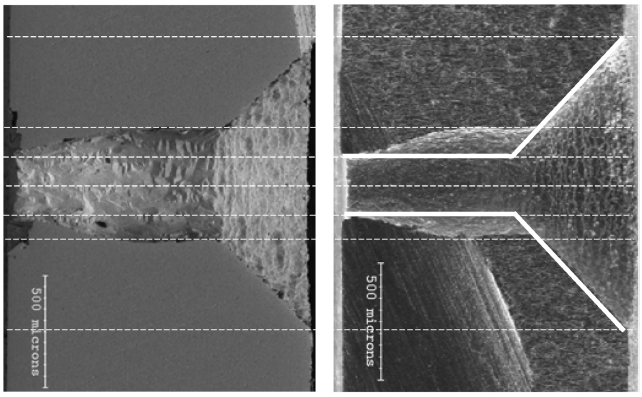

Fig. 2 Photographs of the eroded orifice channel in two neutralizer hollow cathodes after the completion of two 30-cm ion engine life tests. The original orifice radius was 140 μm. The Extended-Life Test (left) accumulated 30,352 h and was operated at various throttle levels. The Life Demonstration Test (right) accumulated 8192 h and was operated at the full-power throttle level. The thick (white) line indicates the shape of the orifice at beginning of life. The dashed lines are added to better illustrate the similarity of the erosion profiles by the end of the two tests.

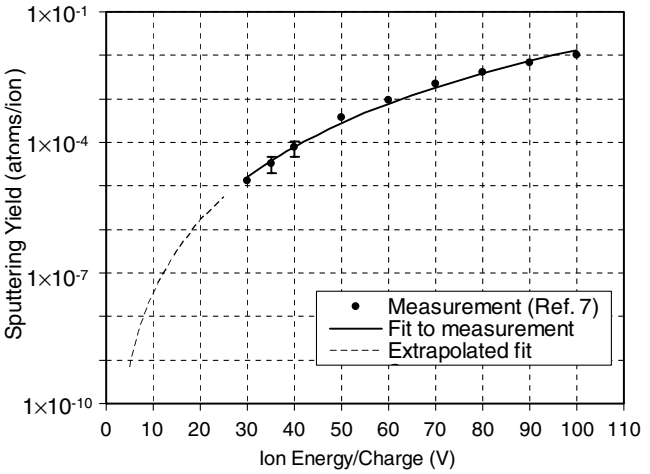

Fig. 3 Sputtering yield for *W* as a function of Xe-ion energy per charge.

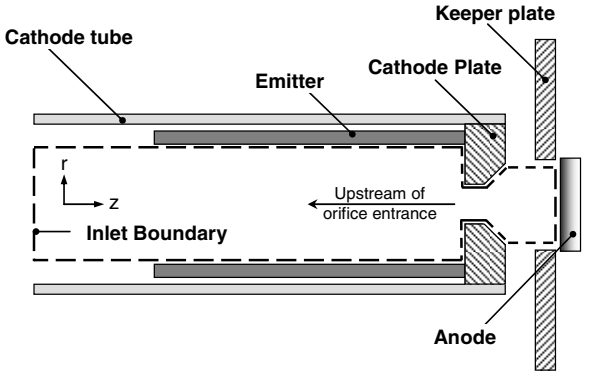

Fig. 4 Schematic of the hollow cathode (not to scale). The dashed line outlines the computational region used in the numerical simulations.

simulations showed that the region of interest, namely, the orifice channel, was unaffected by the addition of a cathode plume region. Thus, to reduce computational times, a plume region is excluded and the current is collected at a virtual anode placed at the keeper exit. Also, the gap between the keeper and cathode plates is not modeled; the imposed boundary conditions assume that the plate wall covers the gap. The global grid arrangement is shown in Fig. 5 (top). The bottom of Fig. 5 is a close-up of the orifice and keeper channel regions illustrating the stepped-grid arrangement constructed to emulate the chamfered region of the cathode orifice. It is noted that the minimum grid size is much larger than the Debye length, which can be as small as a tenth of a micron in the NHC orifice. Thus, the effect of the sheath on the plasma solution is accounted for through the boundary conditions, which are based on the thin-sheath approximation.

The conservation laws for the partially ionized gas, Eqs. (2–9), and related boundary conditions have been presented in detail in previous papers [8,9] and will only be described briefly here. In the 2-D model, the equations of continuity and momentum for ions [Eqs. (2), (6), and (4), respectively], and the momentum equation for the electrons [Eq. (4)], are solved directly to yield the plasma particle density, ion, and electron current densities. The combination of the electron and ion continuity equations yields the current conservation law [Eq. (7)], which is solved for the plasma potential. The model accounts for singly charged (Xe^+) ions only. In the region of highest plasma densities, that is, in the NHC orifice, the ionization rate for Xe^{++} is found to be at least 100 times smaller than the Xe^+ rate based on measured [10] ionization cross section for the $e + Xe^+ \rightarrow Xe^{++}$ reaction. Because the deviation between the two ionization cross sections increases steeply with decreasing electron temperature, the large discrepancy between the two rates is largely due to the low electron temperatures attained inside the orifice, which do not exceed ~2 eV.

The electron temperature is obtained from the electron energy transport equation [Eq. (8)]. The energy equation includes thermal

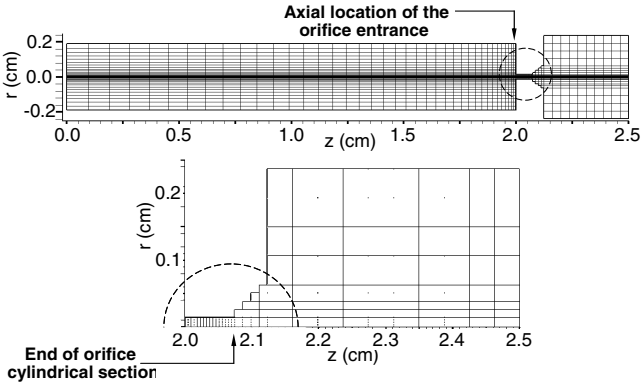

Fig. 5 Computational grid arrangement used in the numerical simulations of the NHC.

diffusion, energy losses due to ionization, and the work done on the electrons by the electric field. The ions and neutrals are assumed to be in thermal equilibrium at temperature T_h, and a single equation is employed for the conservation of energy of the heavy species. In the numerical model, it is the sum of the transport Eqs. (9a) and (9b) that is in fact solved. Dirichlet boundary conditions are assumed for Eqs. (9a) and (9b) with the orifice plate temperature set equal to the peak emitter temperature. Although the keeper plate temperature is only crudely estimated to be 500°C, the orifice results presented herein are not found to be critically sensitive to this value. Sheath boundary conditions are applied at the cathode wall boundaries that include thermionic emission from the emitter based on a prescribed temperature profile. Previous simulations of the DHC employed a profile that was obtained by direct measurement [11]. No such measurements exist for the NHC. The emitter temperature has therefore been approximated based on the DHC measurements at different currents and flow rates. To assess the sensitivity of the emission characteristics on the emitter, temperature simulations at two different peak temperatures have been performed.

The neutral gas density is determined by the neutral gas continuity equation [Eq. (3)], which includes the ionization source term $\dot{n}$. Inside the cathode, the neutral gas satisfies the continuum assumption so the fluid momentum equation [Eq. (5)] is solved to yield the neutral gas flux. The (viscous) Reynolds number for the NHC orifice flow is found to be in the order of unity, and so, in principle, viscous effects should not be neglected. The addition of the viscous terms in the neutral gas conservation laws and the effects of viscosity is a topic of ongoing investigation by the authors [12]. Preliminary simulation results of the DHC interior, where the Reynolds number is also found to be in the order of unity, show that viscosity leads to higher cathode pressure. In regards to the plasma, it is observed that its qualitative behavior remains largely unaltered although some quantitative differences are obtained. For example, the peak plasma density in the DHC interior is found to be about 50% higher when neutral gas viscosity is included with almost no change in the plasma potential at the same location. Similar trends are expected in the NHC, which would lead to a higher erosion rate than presently predicted by the inviscid solution. As it will be shown later in this paper, the predicted erosion as a function of time suggests an asymptotic value that underestimates the observation by about 10%, which could be due to the under prediction of the plasma density as a result of the absence of the neutral gas viscosity. By excluding the relevant terms in the present simulations, however, the effect(s) of viscosity may not yet be quantified.

For the cathode studied here, the mean free paths (mfp) for neutral collisions are found to be comparable to the characteristic dimensions inside the cathode orifice and can be many times the keeper diameter in the keeper orifice region. For the simulation of the rarefied-gas regions, it is customary to implement particle methods such as direct Monte Carlo simulation (DSMC) or particle-in-cell (PIC). In the highly collisional region of the NHC studied here, particle methods would require an excessive number of particles and, consequently, long computational times. Because of the large system of equations that must be solved in the hollow cathode, computationally inexpensive approaches must be devised that sacrifice some accuracy for the sake of computational speed and smoothness of the solution. In the model, we assume that the gas particles expand freely in straight-line trajectories from a predetermined boundary, the "transition line," which is chosen in the present simulations to be at the exit of the cylindrical orifice section of the cathode. Beyond this line, a collisionless region is assumed for the neutrals. The fundamental assumption in this region is that the gas emanates from surfaces with a positive normal velocity and a thermal spread perpendicular to that surface. Then, at large distances from the surface, the spread of the perpendicular velocity is reduced due to geometrical selection. The flux of particles is thus only altered by either an ionization event or an encounter with walls. Particles impacting the walls are assumed to return back to the computational region with a thermal speed that is determined based on the local wall temperature. Under these assumptions, the problem then becomes one of computing all the geometrical view factors (but only once) and keeping track of particle fluxes associated with the various wall boundaries. Because the approach relies heavily on the determination of all view factors associated with the cathode geometry, we will refer to this approach as the VF (view factor) method. The collisionless region is "fed" with the solution of the fluid momentum equation inside the cathode. The two regions comprising fluid and collisionless neutrals are coupled at the transition line.

$$\frac{\partial n}{\partial t} + \nabla \cdot (n\mathbf{u}_i) = \dot{n} \tag{2}$$

$$\frac{\partial n_n}{\partial t} + \nabla \cdot (n_n\mathbf{u}_n) = -\dot{n} \tag{3}$$

$$0 = ne\mathbf{E} - \nabla p_i - nM[\nu_{ie}(\mathbf{u}_i - \mathbf{u}_e) + \nu_{in}(\mathbf{u}_i - \mathbf{u}_n)] \tag{4}$$

$$\frac{\partial (Mn_n\mathbf{u}_n)}{\partial t} + \nabla \cdot (Mn_n\mathbf{u}_n\mathbf{u}_n) = nM\nu_{in}(\mathbf{u}_i - \mathbf{u}_n) - \nabla p_n \tag{5}$$

$$0 = -ne\mathbf{E} - \nabla p_e - nm_e[\nu_{ei}(\mathbf{u}_e - \mathbf{u}_i) + \nu_{en}\mathbf{u}_e], \qquad \mathbf{u}_e \gg \mathbf{u}_n \tag{6}$$

$$\nabla \cdot (\mathbf{j}_e + \mathbf{j}_i) = 0 \rightarrow \nabla \cdot \left[\frac{\nabla\phi}{\eta} - \frac{\nabla p_e}{\eta en} - \mathbf{j}_i\left(1 - \frac{\nu_{ei}}{\nu_{en} + \nu_{ei}}\right)\right] = 0$$
$$\eta = \frac{m_e(\nu_{en} + \nu_{ei})}{\eta e^2} \tag{7}$$

$$\frac{3}{2}\frac{\partial p_e}{\partial t} - \nabla \cdot \left(\frac{5}{2}T_e\mathbf{j}_e + \kappa_e\nabla T_e\right) = Q_e^R + Q_e^T - \mathbf{j}_e \cdot \frac{\nabla p_e}{en} - \dot{n}e\varepsilon_{\text{ip}} \tag{8}$$

$$\frac{3}{2}\frac{\partial p_i}{\partial t} + \nabla \cdot \left(\frac{5}{2}p_i\mathbf{u}_i - \kappa_i\nabla T_i\right) = Q_i^R + Q_i^T + \mathbf{u}_i \cdot \nabla p_i \tag{9a}$$

$$\frac{3}{2}\frac{\partial p_n}{\partial t} + \nabla \cdot \left(\frac{5}{2}p_n\mathbf{u}_n - \kappa_n\nabla T_n\right) = Q_n^R + Q_n^T + \mathbf{u}_n \cdot \nabla p_n \tag{9b}$$

$$\begin{aligned}
Q_e^R &= \left(\mathbf{E} + \frac{\nabla p_e}{en}\right) \cdot \mathbf{j}_e \\
Q_e^T &= -3en\frac{m_e}{M}(\nu_{ei} + \nu_{en})(T_e - T_h) \\
Q_i^R &= -n[m_e\nu_{ei}(\mathbf{u}_e - \mathbf{u}_i) - M\nu_{in}(\mathbf{u}_i - \mathbf{u}_n)] \cdot \mathbf{u}_i \\
Q_i^T &= -3en\frac{m_e}{M}\nu_{ei}(T_h - T_e) \\
Q_n^R &= -n[m_e\nu_{en}\mathbf{u}_e + M\nu_{in}(\mathbf{u}_i - \mathbf{u}_n)] \cdot \mathbf{u}_n \\
Q_n^T &= -3en\frac{m_e}{M}\nu_{en}(T_h - T_e)
\end{aligned} \tag{10}$$

It is assumed that the heavy species reach thermal equilibrium at temperature $T_h = T_i = T_n$ much faster than ions with electrons. Thus, the frictional and thermal heating terms are given by Eqs. (10). The conservation equations are descretized using finite volumes. All vectors are defined at cell edges and all scalars are defined at cell centers. The system is solved in a time-split manner. The plasma equations are solved using a strongly implicit method. The neutral gas continuity and momentum equations are solved explicitly. The numerical approach for the neutral gas fluid momentum equation uses an upwind finite volume scheme by applying Godunov's [13] first-order upwind fluxes across each edge with no flux limiting.

IV. Numerical Simulation Results

A. Sensitivity Calculations

The hollow cathode model requires that the temperature of the emitter be specified. In past numerical simulations of different cathodes, whenever a direct measurement was available, it was implemented directly into Richardson's relation for thermionic emission. Richardson's relation is the emission boundary condition used in the model, and its implementation has been described with greater detail in a previous paper [8]. The specification of the emitter temperature in the model requires two inputs: the peak emitter temperature $T_{w,\max}$ (in K) and a nondimensional polynomial that expresses the variation of the temperature as a function of position along the emitter in the form of

$$T_w \equiv T_{w,\max} + c_1 L_{\text{ins}}(\bar{z}-1) + c_2 L_{\text{ins}}^2(\bar{z}^2-1) + c_3 L_{\text{ins}}^3(\bar{z}^3-1) + c_4 L_{\text{ins}}^4(\bar{z}^4-1) \qquad (11)$$
$$\bar{z} \equiv z/L_{\text{ins}}$$

In the DHC, T_w has been measured [11] for various operating conditions and has been prescribed in the model using specific values of the constants c. During high-power thruster operation, the maximum and minimum temperatures along the insert were approximately 1474 and 1300 K, respectively. No such measurement exists for the NHC. Using the measured temperatures of the DHC emitter as a function of discharge current [11], the $T_{w,\max}$ in the NHC is estimated to be approximately 200 K colder, assuming that its dependence on the flow rate is weak. For the temperature boundary condition in the present NHC calculations, $T_{w,\max}$ is set to 1274 K, and the variation with distance is set to the DHC profile measured during high-power cathode operation. The strong dependence of Richardson's equation on the temperature warrants a sensitivity calculation that quantifies our uncertainty in the emitter temperature on the solution of the orifice channel plasma and ultimately on the erosion predictions. In Fig. 6, the plasma density and potential along the axis of symmetry inside the NHC orifice are compared for three simulation cases: $T_{w,\max}$, $T_{w,\max}+50$ K, and $T_{w,\max}$-50 K. It is found that the effect of the emitter temperature on the plasma density (Fig. 7) and on the neutral gas density (Fig. 7) is not significant. A difference of $\sim$1 V for the $T_{w,\max}+50$ K case and $\sim$5 V for the $T_{w,\max}$-50 K case are computed for the plasma potential (Fig. 7). For a singly charged ion bombarding a W surface with energy that equals the computed plasma potential, a value that is lower by 1 V implies factors of 1.2–1.6 lower sputtering yield, based on Fig. 3. For values higher by 5 V, the range is much greater, 3.2–9 higher sputtering yield. These values are identified as the uncertainties in our numerical results.

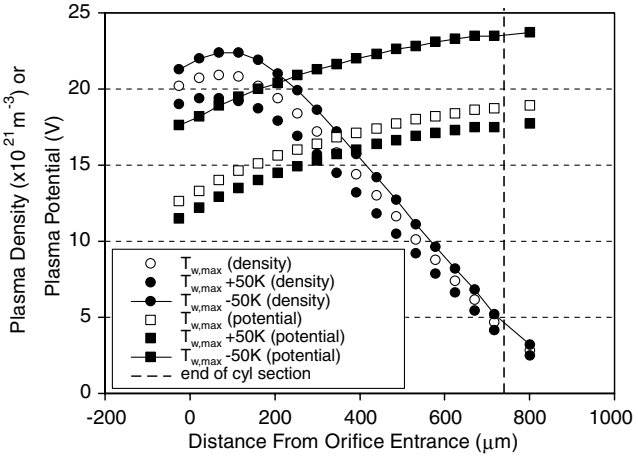

Fig. 6 Sensitivity of the plasma density and potential on the emitter temperature. The vertical dashed line indicates the end of the orifice's cylindrical section.

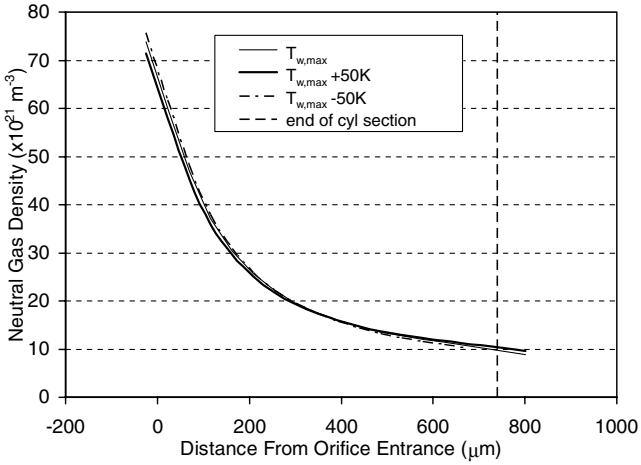

Fig. 7 Sensitivity of the neutral gas density on the emitter temperature.

B. Partially Ionized Gas Inside the Cathode Orifice

1. Plasma Flow Inside the Orifice

Inside the channel, the two critical plasma quantities associated with erosion are the plasma potential and the ion flux. The photographs of the eroded channel (Fig. 2) show little to no erosion at the orifice entrance but show significant erosion at the end of the orifice where the channel opened up to approximately twice its original size. This implies that the plasma potential, the dominant driver of the channel erosion, rises along the channel. At the beginning of the channel, the numerical simulations show that this rise is driven mainly by the resistive contribution to the electric field. The pressure-gradient force rises in magnitude along the channel and ultimately balances the resistive force at the end of the channel. The maximum value that the plasma potential attains inside the channel relative to the value at the orifice entrance is determined by the balance between these two forces. To better illustrate this, the electron momentum Eq. (6) is written in the form of Ohm's law as follows:

$$\mathbf{E} = \eta \mathbf{j}_e - \frac{\nabla p_e}{ne} + \frac{m_e \nu_{ei}}{ne^2}(en\mathbf{u}_i) \qquad (12)$$

Then, the plasma potential in the axial direction (z) is determined by

$$\nabla\phi \approx -\eta j_{e,z} + \frac{\nabla p_e}{ne} - \frac{m_e \nu_{ei}}{ne^2}(enu_{i,z}) \qquad (13)$$

$$(i) \qquad (ii) \qquad (iii)$$

and the solution is shown in the lower part of Fig. 8. The dominance of terms (i) and (ii) in Eq. (13) is clearly seen in Fig. 9, which compares all three terms along the centerline. It is noted that because the density peaks *inside* the orifice, the pressure-gradient force in fact complements the resistive force. It is not until the last $\sim$100 μm of the cylindrical section that the pressure-gradient overtakes the resistive force and drives the observed reduction of the plasma potential downstream of the channel.

At the channel wall, the sheath boundary condition for the electrons is implemented as follows:

$$\mathbf{j}_e \cdot \hat{\mathbf{n}} = -j_{e,\text{th}} \exp\lfloor -e(\phi_p - V_c)/k_B T_e \rfloor \qquad (14)$$

where $\phi_p - V_C$ is the voltage drop across the sheath. In all simulations presented in this paper, $V_C = 0$. As a result of the high plasma potential values near the wall, the loss of electron flow to the surface is negligible compared with the axial flow. It is found that the total electron current lost to the cylindrical wall section is only 92 mA compared with the neutralizer current of 3.26 A. The electron flow established inside the channel is found to be strongly one-dimensional (Fig. 8, top half), and the resistivity is found to be fairly constant. The latter is because the $e-i$ collision frequency

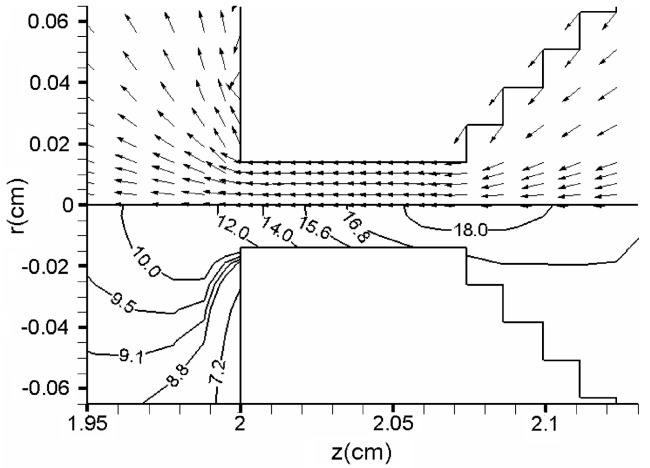

Fig. 8 Electrical properties of the plasma in the NHC orifice region. Top half: electron current density unit vectors $\mathbf{j}_e/|\mathbf{j}_e|$, where $\mathbf{j}_e = -en\mathbf{u}_e$ (note that the direction of the electron flow is opposite to the direction of $\mathbf{j}_e$). Bottom half: plasma potential contours in volts.

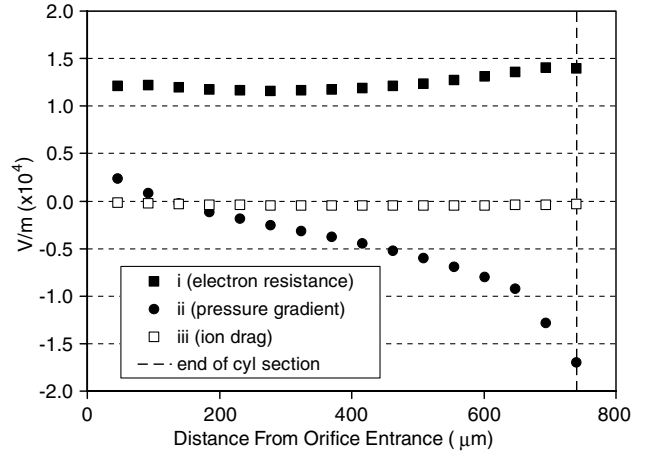

Fig. 9 The comparison of terms in Ohm's law [Eq. (13)] shows that the potential rise along the orifice channel is driven by the (competing) electron resistance and pressure gradient.

dominates over the $e - n$ collision frequency in this region as shown in Fig. 10. Thus, the resistivity scales with $T_e^{-3/2}$, which varies by a maximum of only ~15% inside the channel.

By contrast to the electron flow, the ion flow is found to be purely two-dimensional. The unit ion flux vectors inside the orifice are shown in Fig. 11. Equations (3) and (4) are the main conservation laws for the determination of the ion flow. A comparison of all the forces that act on the ions is presented next. It is shown that the neutral gas drag force dominates along the axis of symmetry whereas the (radial) Bohm ion flux dominates near the channel wall.

Equation (4) may be rewritten as follows:

$$(Mv_{in} + m_e v_{ei})n\mathbf{u}_i \approx Mv_{in}n\mathbf{u}_i$$
$$= ne\mathbf{E} - \nabla p_i - e^{-1}m_e v_{ei}\mathbf{j}_e + Mv_{in}n\mathbf{u}_n \qquad (15)$$

The ion pressure-gradient term is dominated by the plasma density gradient. Thus, the ion flux in the axial direction may be approximated by

$$nu_{i,z} \approx \frac{ne}{Mv_{in}}E_z - \frac{eT_h}{Mv_{in}}\nabla_z n - \frac{m_e}{M}\frac{v_{ei}}{v_{in}}e^{-1}j_{e,z} + nu_{n,z} \qquad (16)$$

$$(I) \qquad (II) \qquad (III) \qquad (IV)$$

The four terms on the right-hand side of Eq. (16) are plotted in Fig. 12.

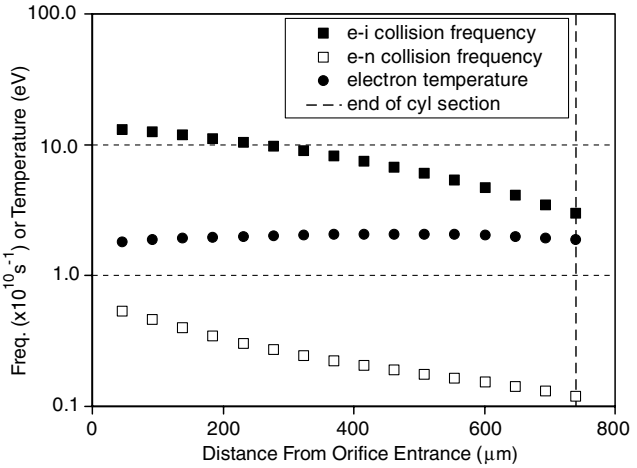

Fig. 10 Classical collision frequencies and temperature for electrons along the centerline.

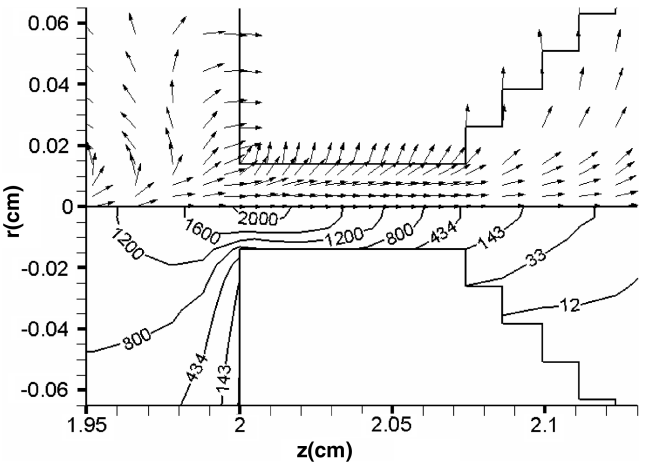

Fig. 11 Ions in the NHC orifice region. Top half: ion flux unit vectors $n\mathbf{u}_i/|n\mathbf{u}_i|$. Bottom half: plasma density contours in $n \times 10^{19}$ m^{-3}.

At the channel wall, the sheath boundary condition for the ions is implemented as follows:

$$(n\mathbf{u}_i) \cdot \hat{\mathbf{n}} = n_p \exp(-\tfrac{1}{2})\sqrt{eT_p/M} \qquad (17)$$

where the plasma density at the grid cell center adjacent to the wall boundary is denoted by n_p. Equation (17) enforces the Bohm

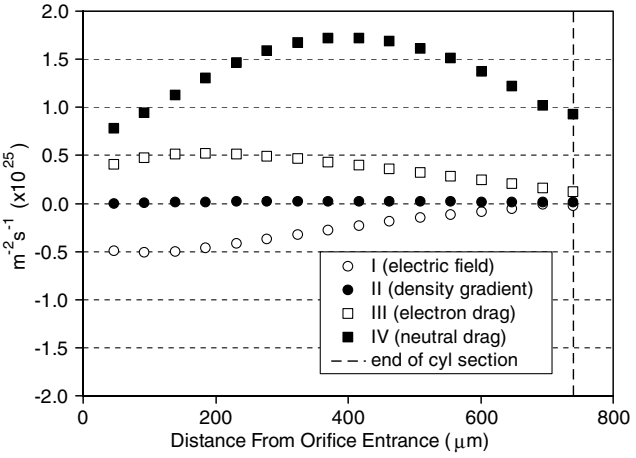

Fig. 12 The comparison of terms in the ion momentum equation shows that ions are largely "dragged" by the neutral gas flow along the centerline, while the electric field acts as the opposing force.

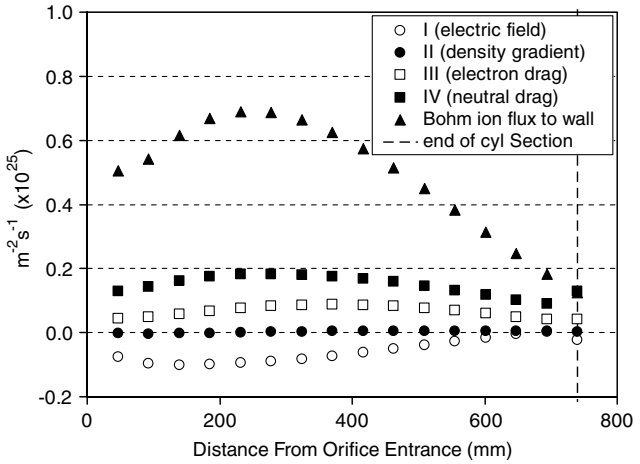

Fig. 13 Comparison of terms in the ion momentum equation near the walls showing that ions are largely driven by the (radial) Bohm ion flux along the channel wall, while the remaining (axial) forces almost cancel each other.

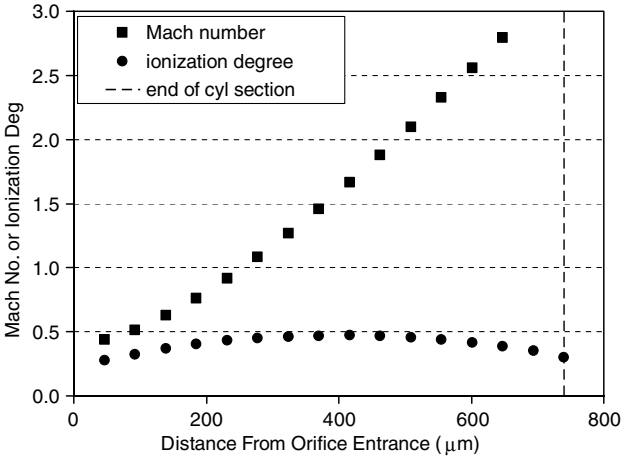

Fig. 15 Mach number $u_{n,z}/(5/3eT_h/M)^{1/2}$ and degree of ionization $n/(n_n + n)$ along the centerline of the NHC orifice.

condition at the wall boundaries when T_p is taken as the value of the electron temperature at the adjacent grid cell center. The comparison of the ion flux terms in Fig. 13 shows that ions are largely driven by the (radial) Bohm ion flux along the channel walls, whereas the remaining (axial) forces almost cancel each other. This cancellation of forces leads to the two-dimensional nature of the ion flow inside the channel, as illustrated in Fig. 11. The results of Figs. 12 and 13 emphasize the importance of the neutral gas flow and the wall boundary conditions on the ion flow inside the orifice.

2. Neutral Gas Flow Inside the Orifice

As with the ion flow the neutral gas inside the orifice channel is also two-dimensional. It exhibits large variations in density (Fig. 14) and the Mach number range is 0.5–3 (Fig. 15) with T_h ranging from 4400 to 2100 K based on the numerical results. Thus, from a continuum point of view, the computed Mach numbers imply that the neutral gas flow is compressible. In reality, the Knudsen number defined here simply as $Kn = \lambda_{n-\alpha}/2r_o$ ranges from 0.15 at the entrance of the cylindrical section to 0.9 at the exit, and can exceed unity in the chamfered region of the orifice (see Fig.16). Thus, another major difficulty in modeling the gas is that the flow falls neither under the continuum regime nor under the free-molecule regime. Such transitional flow presents difficulties not only regarding the numerical aspects of the problem but also from a physical standpoint; for example, the viscous boundary layer as defined conventionally in Newtonian fluid mechanics begins to lose its identity as the flow transitions from continuum to free molecule.

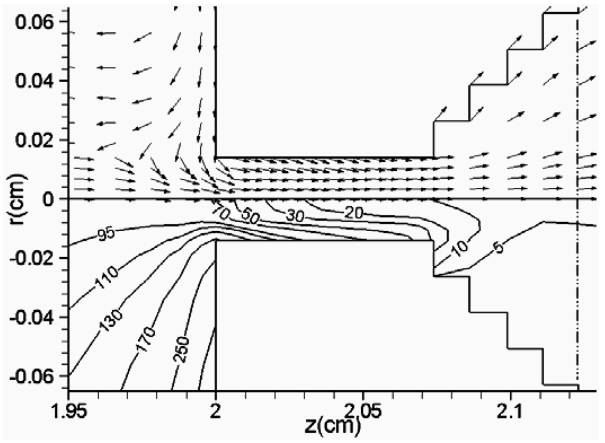

Fig. 14 Neutrals in the NHC orifice region. Top half: particle flux unit vectors $n_n u_n/|n_n u_n|$. Bottom half: particle density contours in $n_n \times 10^{21}$ m^{-3}. The dashed-dot-dot line indicates the location where the neutral gas model transitions from the continuum approach to the collisionless method.

A major goal of the work presented in this paper is to identify the driving mechanism(s) of channel erosion. Because of the sensitivity of the erosion rate on the ion energy (see Fig. 3), it is critical that the method used to model the neutral gas does not introduce nonphysical features in the plasma properties, especially in the plasma potential. Both the inherently "noisy" nature of particle methods, as well as the computational intensity that would be required for these methods inside the cathode, have led us to exclude them as options. Equivalently, any approach that attempts to link different numerical methods, such as, for example, continuum to DSMC or continuum to VF, must ensure that the transition boundary introduces no artificial discontinuities in regions of the plasma where erosion can be significant.

The approach followed here is to solve the fluid laws for the gas inside the orifice and place the continuum-to-VF transition line at the exit of the chamfered region, as shown in Fig. 14. Several studies on the modeling of transitional flows have proposed that the generalized hydrodynamic models such as the Navier–Stokes can be augmented with higher-order terms to include transition-flow effects. Some of these models are the Burnett equations [14], 13-moment Grad's equations [15], Gaussian closure or Levermore moment equations [16], Eu's equations [17], etc., and these have been tested (in many cases extensively) by various authors. For example, extensive numerical simulations performed by Agarwal et al. [14] showed that for subsonic and supersonic flows through channels with $0.1 < Kn < 0.7$ the Navier–Stokes, Burnett, and DSMC solutions were within $\sim$20% in the main flow although the discrepancy could be more than 50% near the walls. Because of the complexity and size of the systems of equations that must be solved for the partially ionized gas in cathodes, and in light of the uncertainties associated with the sputtering yield data, our approach sacrifices the improved accuracy of higher-order hydrodynamic models for the sake of simplicity and computational speed.

In regard to viscous effects, a boundary layer is formed because particles reflect off "rough" surfaces and loose momentum. From the continuum perspective, this process leads to a reduction of the effective fluid velocity from the freestream to the wall. In computational hydro/magnetohydrodynamic flows, it is customary to implement "no-slip" or "free-slip" boundary conditions on the velocity (depending on the Reynolds number), if the Knudsen number is low enough, and include the appropriate viscous terms in the momentum equation to account for the shear forces on the fluid element. In the present problem, the continuum approximation is challenged, a portion of the neutral particles can in fact be lost (or "stick") to the surface, whereas an ion bombarding the surface can pick a free electron from the surface and return back to the flow as a neutral atom. Because the neutral gas and ion plasma densities in the channel are comparable (compare Figs. 11 and 14 or see degree of

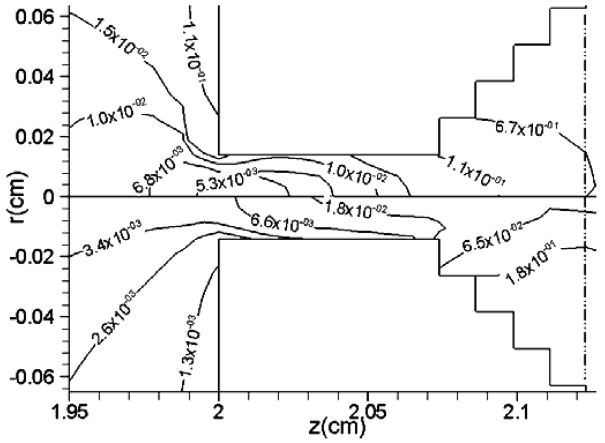

Fig. 16 Characteristic mean free paths $\lambda_{n\alpha} \equiv 1/n_\alpha \sigma_{n\alpha}$ (in cm) for neutral collisions with target particles α. Top half: $\alpha =$ ions ($\sigma_{ni} = \sigma_{CEX} = 10^{-18}$ m^2). Bottom half: $\alpha =$ neutrals ($\sigma_{nn} \approx 0.3\times 10^{-18}$ m^2).

ionization in Fig. 15), it is assumed here that the latter effect (i.e., ions returning from the surface as neutrals) is dominant in the development of the boundary layer. We arrive at this conclusion because the flux of ions striking the surface is much greater than the flux of neutrals to that surface because the sheath accelerates ions but neutrals are unaffected by it. It is further assumed that all ions striking the surface return as neutrals, and so the flux boundary condition at the channel wall becomes

$$(n_n \mathbf{u}_n) \cdot \hat{\mathbf{n}} = -(n\mathbf{u}_i) \cdot \hat{\mathbf{n}} \tag{18}$$

Equations (5) and (18) lead to the neutral flux field shown in Fig. 14. As a final note, it should be recognized that the effects of viscosity may be quantified only if the appropriate terms in the neutral gas conservation laws are included; this is the subject of ongoing work by the authors [12].

C. Channel Erosion

When ions strike the interior of a cylindrical channel of length Δz and radius r_o, the number of atoms sputtered off the surface in a given time interval Δt is given by

$$2\pi r_o \Delta z (n u_{i,\perp}) Y \Delta t, \qquad u_{i,\perp} = \mathbf{u}_i \cdot \hat{\mathbf{n}} \tag{19}$$

where $Y = Y(\varepsilon_i)$ is the sputtering yield of the material. For tungsten, Y was plotted as a function of Xe-ion energy ε_i (per charge) in Fig. 3. Because the number of W atoms in an element of volume is given by

$$\frac{\rho N_{\mathrm{AV}}}{AW} \Delta z \pi (\Delta h^2 + 2 r_o \Delta h) \tag{20}$$

the ratio of the erosion depth (or height) Δh over the (original) radius may be expressed as

$$\frac{\Delta h}{r_o} = \sqrt{1 + \frac{2\Delta t}{r_o} \frac{AW}{\rho N_{\mathrm{AV}}} (n u_{i,\perp}) Y} - 1 \tag{21}$$

Assuming that only singly charged ions with energy $\varepsilon_i = e\phi_p$ strike the surface the instantaneous erosion rate $\Delta h/\Delta t$ at $t = 0$ h, based on the computed plasma properties, is shown in Fig. 17. It is noted that the initial rate exhibits a nonmonotonic profile along the channel, suggesting that the maximum erosion begun inside the channel rather than at the end of the cylindrical section where the plasma potential is the highest (Fig. 8). The rate is dependent on the product of the ion flux and the yield, and in the NHC channel, the ion flux peaks at approximately the first quarter of the channel. This difference in the location of the potential and density peaks is responsible for the nonmonotonicity of the erosion rate. Although the final erosion profile for the NHC studied here does not exhibit such steep curvature, it should be noted that similar NHCs, such as the one

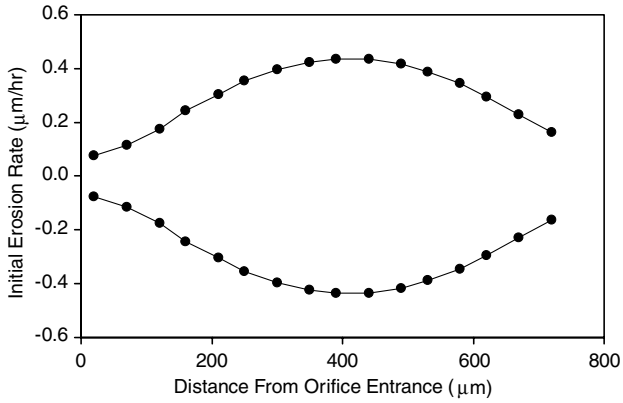

Fig. 17 Computed erosion rate at start of cathode operation.

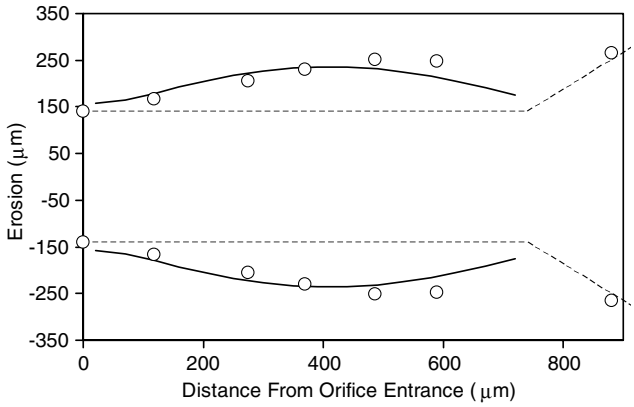

Fig. 18 Erosion depth Δh after 220 h of operation based on the computed initial erosion rate (solid line). The empty circles represent the observed erosion as seen in Fig. 2. The dashed line outlines the original shape of the orifice.

used in Boeing's 13-cm Xenon Ion Propulsion System (XIPS), have produced erosion patterns with a very pronounced peak at about the middle of the orifice channel [‡].

Using the initial rate as shown in Fig. 17, the erosion profile for the NHC studied here is shown in Fig. 18 after 220 h of operation. The mechanism that eroded away the downstream portion of the cylindrical section cannot yet be quantified. It is hypothesized that as the middle of the channel eroded, the current density relaxed, which led to a reduction of the resistive electric field in the region. Thus, the erosion rate likely decreased initially in this region whereas the rate at the end of the cylinder did not change (or increased), which may have led to a gradual flattening of the erosion profile with time. To support this hypothesis, a simulation was performed that incorporated an enlarged portion of the cylindrical section of the orifice, as shown in Fig. 19. The location of the "step" in Fig. 19 is deliberately chosen such that the geometry (crudely) emulates a nonmonotonic erosion profile. Indeed, the computed profiles show a reduction of the erosion rate in the enlarged portion of the orifice and an increase of the erosion rate downstream of this region. The radius of the enlarged portion was set to a few microns larger than the original orifice radius.

To capture the evolution of the plasma self-consistently during the opening of the channel, a dynamical numerical simulation would be required in which the computational grid adapts according to the erosion rate. The nonmonotonic erosion profile shown in Fig. 17 requires that the grid adapts by both creating and eliminating computational cells. In the present study, a dynamical simulation has been performed by adopting an algorithm that only creates new computational cells. Thus, even though the calculation in Fig. 19 provides a hypothesis of how a nonmonotonic initial erosion rate can

[‡]Goebel, D. M., Electric Propulsion Group, Jet Propulsion Laboratory (formerly with Boeing), private communication, Nov. 2006.

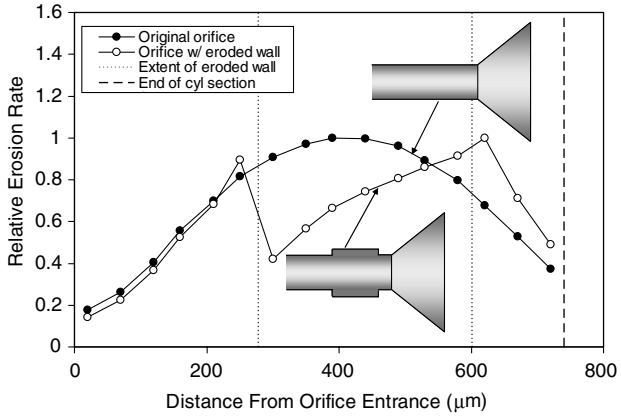

Fig. 19 Effect of nonmonotonic orifice channel geometry on the erosion rate: although the computed maximum of erosion rate peaks initially inside the channel, this maximum rate is reduced as the channel opens. This may have led to the (closely) monotonic profile observed after the life tests, even if the erosion rate at the beginning of the test was nonmonotonic.

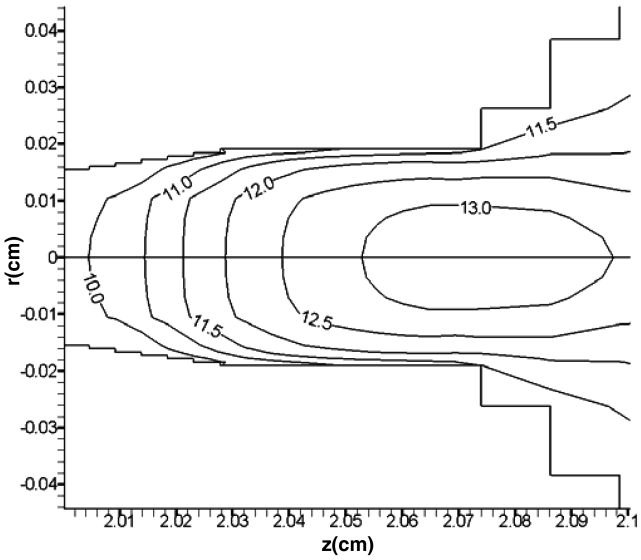

Fig. 20 Plasma potential contours (in volts) in the eroded channel after 500 h of operation.

lead to the observed profile in Fig. 17, it is not yet possible to show this precisely by numerical simulation. It should also be noted that redeposition of sputtered material has not been taken into account in the present simulations.

The adaptive grid algorithm proceeds as follows. First, for a given Δt, the erosion depth Δh is determined along those computational cells that are adjacent to the channel boundary. Then, rows of additional cells are generated in the form of a stepped pyramid. These rows of cells are extended to the downstream boundary of the computational region. Because the algorithm only creates cells, the portion of the erosion rate that predicts a decreasing erosion profile is not modeled; downstream of the location of maximum erosion rate, the erosion height is assumed to remain fixed at the maximum value. At each time increment Δt, the conservation laws for the plasma and neutral gas are solved until a steady-state solution is reached. If the full computational region (Fig. 5, top) was used for these simulations, the calculation would be exceedingly intensive on a single computer processor. Thus, a smaller region has been employed that consists only of the cathode and keeper orifice regions (Fig. 5, bottom). The boundary conditions at the orifice entrance are prescribed as the steady-state solution of the full computational region, and are held fixed during the erosion simulations. This assumption is based on the observation that the channel at the orifice suffered almost no erosion (Fig. 2).

Although the result suggests that all the erosion occurred very early during the life test, it does not provide a good estimate of when the erosion ceased because a single time step cannot resolve the reduction of the erosion rate during the enlargement of the channel. Thus, several simulations were performed at time increments of $\Delta t = 50$ h from 0–50 h, $\Delta t = 100$ h from 100–500 h, $\Delta t = 500$ h from 500–1000 h, and $\Delta t = 1000$ h from 1000–4000 h. An example of the eroded computational region after 500 h of operation depicting the plasma potential is shown in Fig. 20. The maximum erosion depth Δh is plotted as a function of time in Fig. 21. The maximum erosion rate and maximum plasma potential as a function of maximum channel radius are plotted in Fig. 22. The results for the maximum channel radius suggest that the computed erosion would asymptote to a lower value than the observation. For example, at 4000 h, the computed maximum radius is about 10% lower than the observed radius of the cylindrical channel at the end of the life test. The underprediction could be due to several factors, including the exclusion of viscous effects in the neutral gas (which would lead to a higher plasma density inside the orifice), grid resolution, the assumption of nonchanging orifice inlet boundary conditions, the uncertainty in the sputtering yield data, which is in the order of $\pm 40\%$, and the uncertainty associated with our assumed emitter temperature (see Fig. 6). The results also show that more than half of the erosion occurred in less than 1000 h. Considering all the results

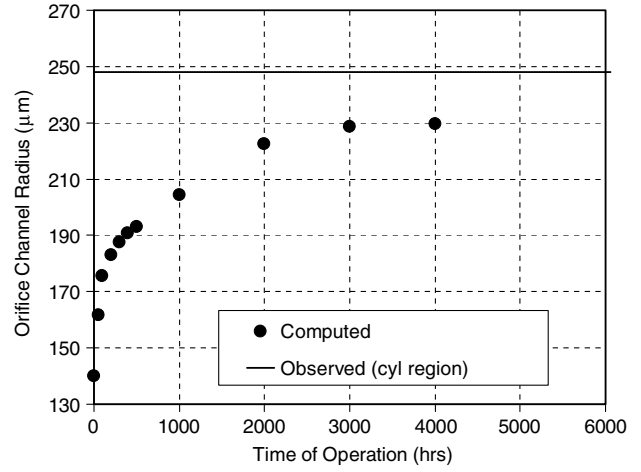

Fig. 21 Maximum orifice channel radius as a function of time.

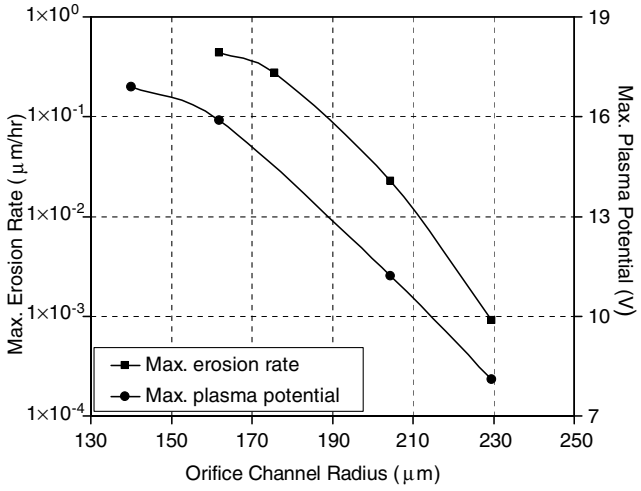

Fig. 22 Maximum erosion rate and plasma potential as a function of channel radius.

and trends presented herein, it is estimated that the erosion shown in Fig. 2 occurred in less than a few thousand hours.

D. Comparisons with the Discharge Hollow Cathode

Whereas the NHC orifice opened significantly during the two life tests, no noticeable erosion of the DHC orifice was observed. No quantitative explanation of this observation has been established since the completion of the two life tests. In this section, a comparison of the simulation results for the two cathodes is performed, and an explanation is provided regarding the erosion trends.

Past numerical simulations of the 30-cm ion engine DHC were performed using a computational region that did not extend beyond the orifice entrance [18]. More recent simulations have extended the computational region to include the cathode and keeper orifices as well as a plume region. It is these more recent simulation results for the DHC that are compared here with the results obtained for the NHC. The steady-state plasma density at TH15 is compared in Fig. 23. By comparison to the DHC, the NHC orifice plasma is at least 40 times as dense, and the maximum plasma potential is 7.0 V higher (Fig. 24). The degree of ionization in the DHC orifice does not exceed 10%. Under such conditions, it is estimated that the erosion rate in the DHC orifice is more than 3 orders of magnitude less than in the NHC orifice, which explains why no noticeable chamfering of the DHC orifice was observed. The large disparity of the conditions attained inside the DHC and the NHC orifices is largely due to the orifice size: the DHC is 3.5 times larger in diameter, and so the current density inside the orifice channel is about three times lower compared with the NHC.

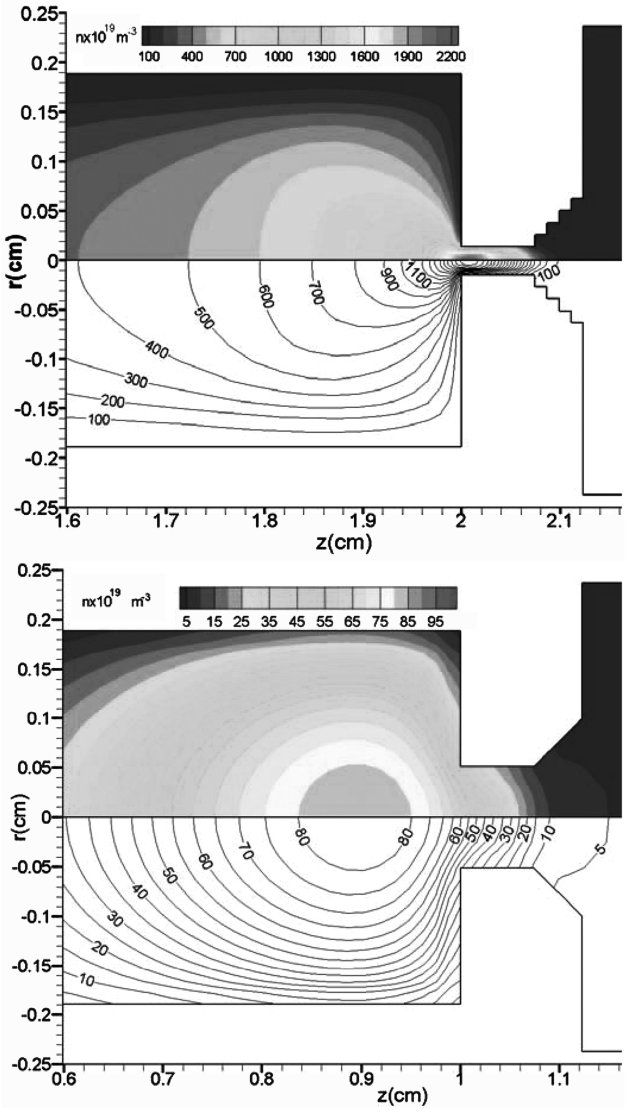

Fig. 23 Comparison of the computed plasma density inside the neutralizer (top) and discharge (bottom) hollow cathodes.

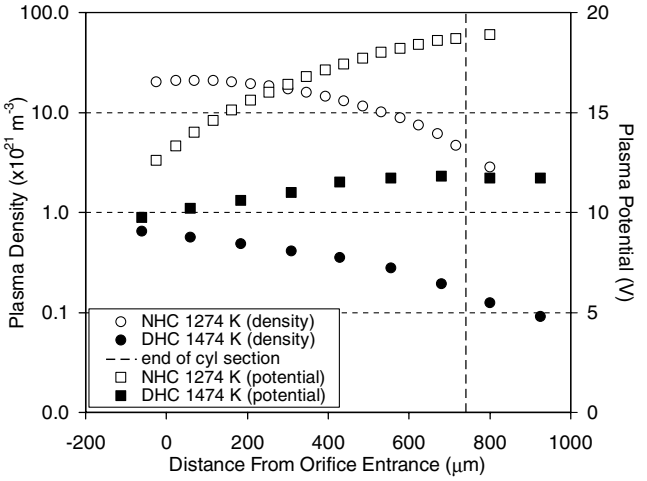

Fig. 24 Comparison of the computed plasma density and potential along the orifice centerline in the discharge and neutralizer hollow cathodes.

V. Conclusions

Two-dimensional simulations of the partially ionized gas in a neutralizer hollow cathode have shown that the flux of Xe^+ and the sheath drop along the orifice channel wall can reach sufficiently high values to cause sputtering of the orifice plate material. By solving numerically a relatively extensive system of conservation laws for the partially ionized gas inside the cathode, and by using recent sputtering yield data at low ion energies, it has been possible to reproduce with good agreement the erosion profile of the orifice observed upon the completion of two long-duration tests that lasted approximately 8200 and 30,000 h, respectively. It has also been possible to provide an explanation for the apparent termination of the erosion and to approximate the time at which it occurred during the tests. As the orifice channel opened due to the erosion, the plasma potential, and, in turn, the energy of the ions bombarding the orifice walls through the sheath, diminished. The maximum energy/charge with which Xe^+ bombarded the orifice walls at beginning of life (BOL) was computed to be about 17 V. By the time the channel opened to a radius of 230 mm, the maximum ion energy had fallen below 9 V, corresponding to almost a 3-orders-of-magnitude drop in the sputtering yield; at such low yields, the erosion is negligible. The results predict that more than one-half of the erosion occurred in less than 1000 h and that the erosion became negligible in less than a few thousand hours. The sputtering yield data obtained by Doerner et al. for $Xe^+ \rightarrow W$ and for $Xe^+ \rightarrow$ Mo (see accompanying paper, "Wear Mechanisms in Electron Sources for Ion Propulsion, 2: Discharge Hollow Cathode") suggest no apparent "sputtering threshold." In the present study, the precipitous drop of the sputtering yield with ion energy for $Xe^+ \rightarrow W$, as predicted by an extrapolation of the available data to the (low) energy values of interest (<30 V), has been sufficient to explain the apparent termination of the NHC orifice erosion with no need to invoke a sputtering threshold. Although the yield data for $Xe^+ \rightarrow$ Mo (obtained for as low as energy/charge = 15 V) strongly support the absence of a threshold, it is recognized by the authors that this argument can be confirmed for $Xe^+ \rightarrow W$ (of interest to this paper) only by additional sputtering yield data that extend to energy/charge $\leq$ 10 V.

A comparison of results between the NHC and the DHC shows that in the DHC orifice the ion density is about 40 times lower, and the maximum sheath drop is 7.0 V lower compared with the values in the NHC. This is because the channel in the DHC is 3.5 times larger in diameter, and so the current density inside the channel is about three times lower compared with the NHC. In turn, the resistive drop

and resistive heating, which largely drive the plasma potential, electron heating, and ionization inside the orifice, are both much higher in the NHC orifice. It is found that the degree of ionization in the NHC orifice can be as high as 50%; in the DHC, it does not exceed 10%. Clogging of the cathode that can potentially occur as a result of the sputtered material can be avoided by manufacturing the cathode with a chamfered channel to minimize erosion. In the 30-cm ion thruster NHC, the chamfered-channel shape would follow the erosion pattern attained at the end of the life test (Fig. 2).

Acknowledgment

The research described in this paper was carried out by the Jet Propulsion Laboratory, California Institute of Technology, under a contract with the National Aeronautics and Space Administration in support of the In-Space Propulsion Technology Program.

References

[1] Polk, J. E., Anderson, J. R., Brophy, J. R., Rawlin, V. K., Patterson, M. J., Sovey, J., and Hamley, J., "An Overview of the Results from an 8200 Hour Wear Test of the NSTAR Ion Thruster," AIAA Paper 99-2446, June 1999.

[2] Sengupta, A., Brophy, J. R., and Goodfellow, K. D., "Status of the Extended Life Test of the Deep Space 1 Flight Spare Ion Engine after 30,352 Hours of Operation," AIAA Paper 03-4558, July 2003.

[3] Mikellides, I. G., Katz, I., Jameson, K. K., Goebel, D. M., and Polk, J. E., "Wear Mechanisms in Electrons Sources for Ion Propulsion, 2: Discharge Hollow Cathode," *Journal of Propulsion and Power*, Vol. XX, No. XX, 2008, pp. XX–XX.

[4] Katz, I., Anderson, J. R., Polk, J. E., and Brophy, J. R., "One-Dimensional Hollow Cathode Model," *Journal of Propulsion and Power*, Vol. 19, No. 4, 2003, pp. 595–600.

[5] Katz, I., Gardner, B. M., Mandell, M. J., Jongeward, G. A., Patterson, M., and Myers, R. M., "Model of Plasma Contactor Performance," *Journal of Spacecraft and Rockets*, Vol. 34, No. 6, 1997, pp. 824–828.

[6] Foster, J. E., and Patterson, M. J., "Downstream Ion Energy Distributions in a Hollow Cathode Ring Cusp Discharge," *Journal of Propulsion and Power*, Vol. 21, No. 1, 2005, pp. 144–151. doi:10.2514/1.4771

[7] Doerner, R. P., "Low-Energy Sputtering Yields of Tungsten and Tantalum," *Journal of Vacuum Science and Technology A (Vacuum, Surfaces, and Films)*, Vol. 23, No. 6, 2005, pp. 1545–1547. doi:10.1116/1.2110385

[8] Mikellides, I. G., Katz, I., Goebel, D. M., and Polk, J. E., "Hollow Cathode Theory and Experiment, 2: A Two-Dimensional Theoretical Model of the Emitter Region," *Journal of Applied Physics*, Vol. 98, No. 11, 2005, p. 113303. doi:10.1063/1.2135409

[9] Mikellides, I. G., Katz, I., Goebel, D. M., and Polk, J. E., "Theoretical Model of a Hollow Cathode Plasma for the Assessment of Insert and Keeper Lifetimes," AIAA Paper 05-4234, July 2005.

[10] Bell, E. W., Djuric, N., and Dunn, G. H., "Electron-Impact Ionization of In+ and Xe+," *Physical Review A*, Vol. 48, No. 6, 1993, pp. 4286–4291. doi:10.1103/PhysRevA.48.4286

[11] Polk, J. E., Marrese, C., Thornber, B., Dang, L., and Johnson, L., "Temperature Distributions in Hollow Cathode Emitters," AIAA Paper 04-4116, July 2004.

[12] Mikellides, I. G., Katz, I., Jameson, K. K., and Goebel, D. M., "Numerical Simulations of a Hall Thruster Hollow Cathode Plasma," International Electric Propulsion Conference Paper 07-018, Sep. 2007.

[13] Godunov, S. K., "A Difference Method for Numerical Calculation of Discontinuous Solutions of the Equations of Hydrodynamics," *Matematicheskii sbornik / izdavaemyi Moskovskim matematicheskim obshchestvom*, Vol. 47(89), No. 3, 1959, pp. 271–306.

[14] Agarwal, R. K., Yun, K., and Balakrishnan, R., "Beyond Navier–Stokes: Burnett Equations for Simulations of Transitional Flows," *Physics of Fluids*, Vol. 13, No. 10, 2001, pp. 3061–3085. doi:10.1063/1.1397256

[15] Roveda, R., Goldstein, D. B., and Varghese, P. L., "Hybrid Euler/Particle Approach for Continuum/Rarefied Flows," *Journal of Spacecraft and Rockets*, Vol. 35, No. 3, 1998, pp. 258–265.

[16] Levermore, C. D., "Moment Closure Hierarchies for Kinetic Theories," *Journal of Statistical Physics*, Vol. 83, Nos. 5–6, 1996, pp. 1021–1065. doi:10.1007/BF02179552

[17] Eu, B. C., *Kinetic Theory and Irreversible Thermodynamics*, Wiley, New York, 1992.

[18] Mikellides, I. G., Katz, I., Goebel, D. M., Polk, J. E., and Jameson, K. K., "Plasma Processes Inside Dispenser Hollow Cathodes," *Physics of Plasmas*, Vol. 13, No. 6, 2006, p. 063504. doi:10.1063/1.2208292

A. Gallimore
Associate Editor